Universiteit Leiden
The Netherlands

Superlattices in van der Waals materials: a low-energy electron microscopy study
Jong, T.A. de

4

INTRINSIC STACKING DOMAINS IN GRAPHENE ON SILICON CARBIDE

Graphene on silicon carbide (SiC) bears great potential for future graphene electronic applications [89–93] because it is available on the wafer-scale [94–97] and its properties can be custom-tailored by inserting various atoms into the graphene/SiC interface [45, 98–103]. It remains unclear, however, how atoms can cross the impermeable graphene layer during this widely used intercalation process [45, 104, 105]. Here we demonstrate that, in contrast to the current consensus, graphene layers grown in argon atmosphere on SiC are not homogeneous, but instead composed of domains of different crystallographic stacking as they have been observed in other systems [47, 106, 107]. We show that these domains are intrinsically formed during growth and that dislocations between domains dominate the (de)intercalation dynamics. Tailoring these dislocation networks, e.g. through substrate engineering, will increase the control over the intercalation process and could open a playground for topological and correlated electron phenomena in two-dimensional superstructures [4, 108–112].

4.1 INTRODUCTION

Graphene can routinely be produced on the wafer scale by thermal decomposition of silicon carbide (SiC) [94–97]. Due to the direct growth on SiC(0001) wafers, epitaxial graphene (EG) naturally forms on a wide band gap semiconductor, providing a doped or insulating substrate compatible with standard CMOS fabrication methods. Hence, EG is a contender for future graphene electronic applications such as power electronics [89, 92], high-speed transistors [90], quantum resistance standards [91] and terahertz detection [93]. In EG, the first hexagonal graphene layer resides on an electrically insulating monolayer of carbon atoms that are sp^3 bonded to silicon atoms of the SiC(0001) surface [94–96, 113]. The presence of this so-called buffer layer strongly affects the graphene on top, e.g. by pinning the Fermi level. Consequently, the graphene properties can be tuned via intercalation of atoms into the buffer layer/SiC interface. The intercalation of hydrogen is most widely used and results in the conversion of the buffer layer to a quasi-freestanding graphene (QFG) layer by cutting the silicon-carbon bonds and saturating silicon dangling bonds with hydrogen. This treatment reverses the graphene doping from n-type to p-type and improves the mobility [44, 45]. Intercalation of heavier atoms is used to further tailor the graphene properties, e.g. to form pn-junctions [98, 101], magnetic moments [102] or potentially superconducting [99] and topologically non-trivial states [100].

It has been realized that the quality of the grown graphene can be greatly improved by reducing the desorption rate of silicon atoms (which allows for a raised growth temperature), for example, by encapsulation of the SiC chip [96], or by growth in low-pressure silane environment [103, 114] or in ambient-pressure argon atmosphere [94, 95]. Graphene (EG and QFG) grown on SiC using these methods appears homogeneous with low defect concentration in most techniques [45, 94–97]. Together with the fact that layers span virtually unperturbed over SiC substrate steps [6, 7, 115], this has led to the consensus of perfectly crystalline graphene. On the other hand, two observations point to a less perfect sheet. First, the charge carrier mobility is generally low, even at cryogenic temperatures [44, 95]. Second, an ideal graphene sheet is impermeable even to hydrogen [104, 105], whereas a wide variety of atomic and molecular species has been intercalated into EG [45, 99–103]. Stacking domains as they have been observed in vacuum-grown graphene on SiC[47] and freestanding bilayer graphene [106, 107] could explain these contradictions. In this Chapter, we demonstrate that graphene grown on SiC in argon atmosphere is, in fact, less homogeneous than widely believed but is fractured into domains of different crystallographic stacking order. We use advanced low-energy electron microscopy (LEEM) methods and *ab initio* calculations to show that those domains are naturally formed during growth due to nucleation dynamics and built-in strain. Their presence is thus intrinsic to all graphene-on-SiC materials, including high-quality graphene grown in argon atmosphere.

4.2 METHODS

4.2.1 SAMPLE FABRICATION

Graphene growth is carried out on commercial 4H-SiC wafers (semi-insulating, nominally on axis, RCA cleaned) at ~1700 °C and 900 mbar Ar pressure for ~30 min as de-

scribed in Ref. [95]. To convert EG to bilayer QFG via hydrogen intercalation, the sample is placed in a carbon container and heated to 970 °C for 90 min at ambient hydrogen pressure as described in Ref. [44, 45]. Samples with small bilayer patches on large substrate terraces are achieved in a three-step process. First, SiC substrates are annealed at ~1700 °C and 900 mbar Ar pressure for 30 min in a SiC container to enable step bunching. Second, unwanted graphitic layers formed during this process are removed by annealing the sample at 800 °C in an oxygen flow for 30 min. Third, graphene growth is carried out as described above.

4.2.2 LOW-ENERGY ELECTRON MICROSCOPY

The LEEM measurements are performed using the aberration correcting ESCHER LEEM facility [26] which is based on a commercial SPECS P90 instrument and provides high-resolution imaging. Limitations on the angles of the incident and imaging beams make dark-field imaging in the canonical geometry, where the diffracted beam used for imaging leaves the sample along the optical axis, impossible. Instead, we use a tilted geometry where the incident angle is chosen such that the specular beam and the refracted beam used for imaging leave the sample under equal, but opposite, angles (illustrated in Fig. 4.1f,i). The tilted incidence yields an in-plane k-vector, which influences the reflectivity spectrum [34, 38]. This is taken into account in our calculations, but needs to be considered when comparing to other LEEM and LEED data. Microscopy is performed below 2×10^{-9} mbar and at 600 °C, to prevent the formation of hydrocarbon-based contaminants under the electron beam. Images are corrected for detector-induced artifacts by subtracting a dark count image and dividing by a gain image as described in the previous chapter before further analysis. Figure 4.4 is corrected for uneven illumination by dividing by the beam profile. Additionally, the minimum intensity in images shown is set to black and maximum intensity is set to white to ensure visibility of all details. In this chapter, all dark-field images and images showing domain walls are integrated for 4 s, all other images for 250 ms.

4.2.3 COMPUTATIONS

All calculations were performed with a full-potential linear augmented plane waves method based on a self-consistent crystal potential obtained within the local density approximation, as explained in Ref. [116]. The ab initio reflectivity spectra are obtained with the all-electron Bloch-wave-based scattering method described in Ref. [117]. The extension of this method to stand-alone two-dimensional films of finite thickness was introduced in Ref. [118]. Here, it is straightforwardly applied to the case of finite incidence angle to represent the experimental tilted geometry. An absorbing optical potential $V_i = 0.5$ eV was introduced to account for inelastic scattering: the imaginary potential $-iV_i$ is taken to be spatially constant over a finite slab (where the electron density is non-negligible) and to be zero in the two semi-infinite vacuum half-spaces. In addition, a Gaussian broadening of 1 eV is applied to account for experimental losses.

4.3 RESULTS

Figure 4.1**a,b** show bright-field LEEM images of two QFG samples with areas of different graphene thickness. Bright-field images are recorded using specularly reflected electrons that leave the sample perpendicular to the surface (see Figure 4.1**c**). The main contrast mechanism in this mode is the interaction of the imaging electrons with the thickness-dependent, unoccupied band structure of the material, which is used to un-
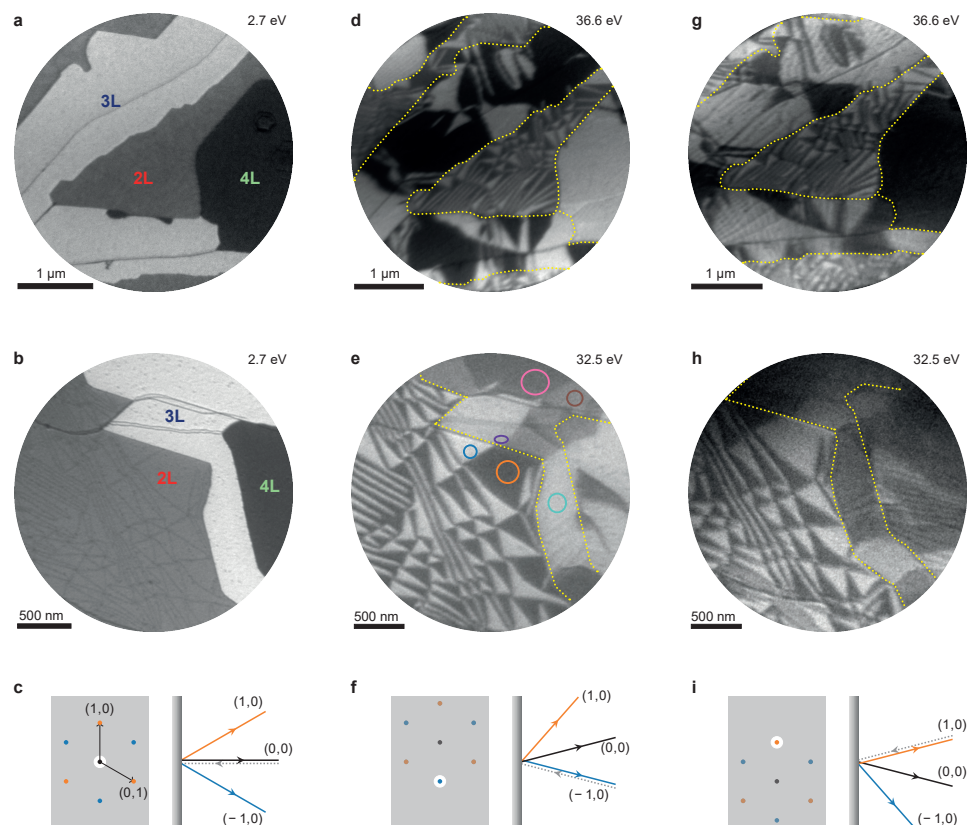

Figure 4.1: Graphene on SiC is composed of domains of different stacking order. a,b, *Bright-field LEEM micrographs of two samples of bilayer, trilayer and four-layer QFG.* **c,** *In bright-field geometry, images are recorded from specularly reflected electrons (black) by selecting the (0,0) diffraction spot using an aperture (gray rectangle) that blocks all diffracted beams (orange and blue).* **d, e,** *Dark-field images of the same area as in a,b. Domains of alternating contrast are clearly visible, indicating areas of different stacking order.* **f,** *Sketch of the tilted dark-field geometry selecting the (−1,0) spot as used for d,e.* **g, h,** *Dark-field images using the inequivalent (1,0) diffraction spot show inverted contrast compared to d,e.* **i,** *Measurement geometry used for g,h. See Methods for details on LEEM imaging modes. Yellow lines in d-h are guides to the eye indicating areas of constant layer number. Circles in e indicate areas from which the spectroscopy data in Fig. 4.2c,d is obtained.*

ambiguously determine the number of graphene layers [30, 38, 46]. Large, homogeneous areas of bilayer, trilayer and four-layer graphene can thus be distinguished in Figure 4.1**a,b**, supporting the notion of perfect crystallinity.

In stark opposition to this generally accepted view, the dark-field images in Figure 4.1**d,e** clearly reveal that all areas are actually fractured into domains of alternating contrast. The symmetry breaking introduced in dark-field imaging, where the image is formed from one diffracted beam only (cf. Figure 4.1**f**), leads to strong contrast between different stacking types of the graphene layers [47, 119]. In fact, the contrast between different domains inverts (Figure 4.1**d,e** versus **g,h**) when dark-field images are recorded from non-equivalent diffracted beams (cf. Fig. 4.1**f** and **i**).

At first glance, the observation of different stacking orders might seem surprising, as it is known that graphene layers grown on SiC(0001) are arranged in Bernal stacking [96]. However, two energetically equivalent versions of Bernal stacking (AB and AC) exist, and have been observed in other graphene systems [47, 106, 107, 120]. The AC stacking order can be thought of either as AB bilayer where the top layer is translated by one bond length, or alternatively, as a full AB bilayer rotated by 60 degrees (Fig. Figure 4.2**a,b**). Consequently, AB and AC stacking are indistinguishable in bright-field imaging. Subsequent layers can be added in either orientation, generating more complicated stacking orders for trilayer and beyond.
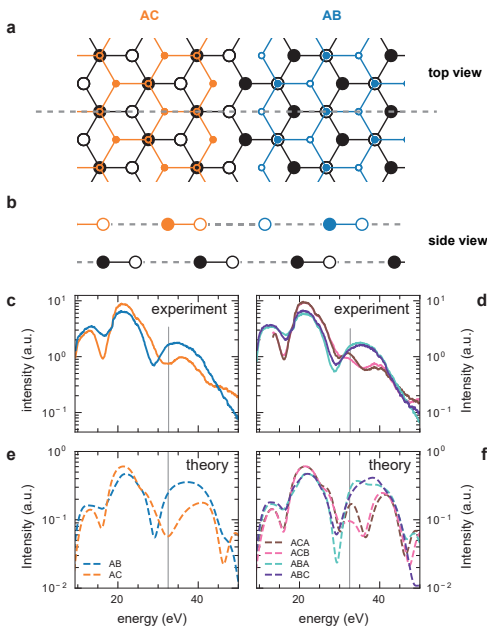

Figure 4.2: Low-energy electron reflectivity spectra reveal the local stacking order. **a,** *Sketched top view illustrating the difference between AC (orange) and AB (blue) stacking orders. Inequivalent atoms of the unit cell of the top layer (orange or blue) sit in the center of the hexagon of the bottom layer (black).* **b,** *Side view of the stacking along the dashed line in (a). Open and closed circles denote the inequivalent atoms of the graphene unit cell.* **c,d,** *Experimental dark-field reflectivity spectra recorded on different stacking domains on bilayer and trilayer graphene, respectively. The areas from which the spectra are recorded are indicated by circles in Fig. 4.1***e***.* **e,f,** *Theoretical dark-field spectra for AB and AC as well as ABA, ABC, ACA and ACB stacking orders obtained by* ab initio *calculations. A Gaussian broadening of 1 eV is applied to account for experimental losses. The vertical lines in* **c** *to* **f** *indicate the landing energy at which Figure 4.1***e,h*** are recorded.*

4.3.1 SPECTROSCOPY

In order to identify the exact stacking in each area, we simulate bilayer and trilayer graphene slabs in different stacking orders and compare their reflectivity with measured low-energy electron reflectivity spectra. The latter are extracted from the intensity of an area in a series of spectroscopic LEEM images recorded at different electron landing energy (see Supplementary Movie 1 and 2 for such measurements of the area in Fig. 4.1**b** in bright-field and dark-field geometry, respectively)[1].
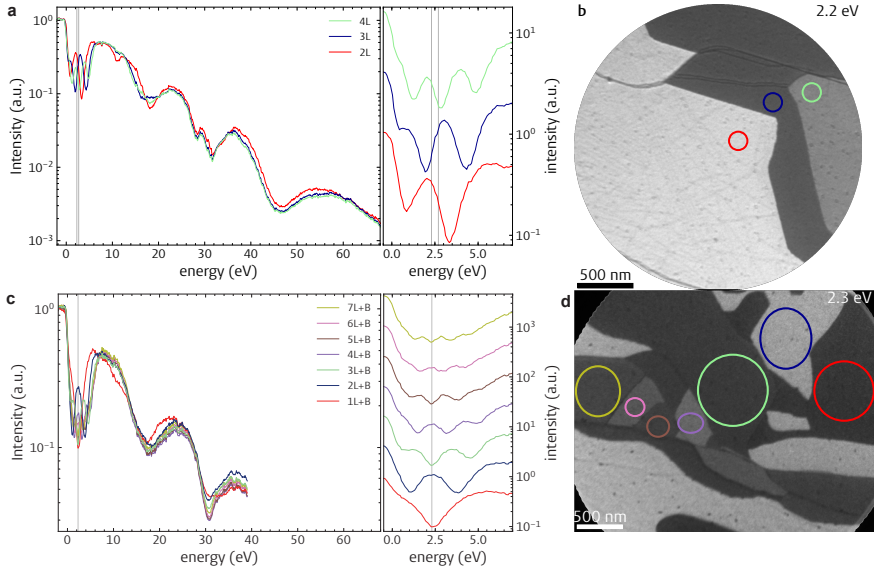

Figure 4.3: a, Bright field intensity curves extracted from the data set of Supplementary Movie 1 (QFG). The minima used to determine graphene layer count are enlarged and offset for clarity on the right. Indicated with gray lines are the landing energies at which Supplementary Movie 3 and Figure 4.1**a,b** are taken. **b,** Same area as Figure 4.1**b**, but rendered at the energy of Supplementary Movie 3 and with the areas used for layer counting indicated. **c,** Bright field intensity curves of a non-intercalated EG sample with 1–7 layers. The minima used to determine graphene layer count are enlarged and offset for clarity on the right. Compared to QFG the minima are slightly shifted [46]. Indicated with gray line is the energy at which Supplementary Movie 3 is taken. **d,** Micrograph of EG sample with the areas used for layer counting in (c) indicated.

While different domains show identical bright-field reflectivity (see Figure 4.3), dark-field spectra extracted from different bilayer domains (marked blue and orange in Fig. 4.2**c** and 4.1**e**) are clearly distinguishable. Moreover, four distinct reflectivity curves are observed for trilayer graphene (Fig. 4.2**d**). Figure 4.2**e,f** shows theoretical dark-field spectra, obtained by *ab initio* calculations (As described in Section 4.2.3), of different bilayer and trilayer stacking orders, respectively. The excellent agreement of theoretical and experimental data in Fig. 4.2**c,e** is clear evidence that the assignment of Bernal AB and AC

---

[1] Supplementary Movies of this chapter are available as Supplementary material to the original publication at http://link.aps.org/supplemental/10.1103/PhysRevMaterials.2.104005 [37]

stacking orders for different bilayer domains is correct. Moreover, the comparison of Fig. 4.2**d** and **f** shows that using these dark-field LEEM methods, we can distinguish the more complicated trilayer stacking orders: Bernal, ABA (cyan) and ACA (pink), versus rhombohedral ABC (purple) and ACB (brown). Due to the small electron penetration depth in LEEM, however, the spectra fall into two families (ABA and ABC vs. ACA and ACB) dominated by the stacking order of the top two layers.
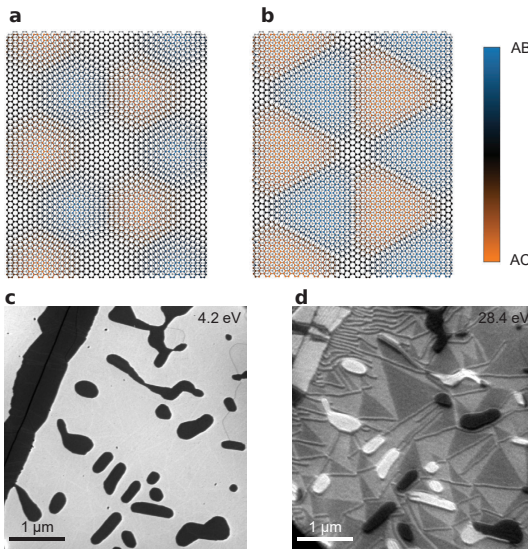
4.3.2 DOMAIN MORPHOLOGY

Figure 4.4: Stacking domains are caused by growth-induced strain and graphene nucleation dynamics. a, *Sketch of bilayer graphene where the top layer is uniformly strained causing a moiré pattern.* **b,** *Sketch of the energetically favored arrangement of AB and AC stacked domains with all strain concentrated into dislocation lines. The trigonal shape of the domains is clearly visible. The color denotes how close a local stacking order is to AB or AC stacking.* **c,** *A bright-field LEEM image of EG where growth was stopped shortly after bilayer starts to form.* **d,** *Dark-field LEEM of the same area reveals that the resulting islands, which emerged from individual nucleation sites, exhibit constant stacking order, i.e. they are either AB (bright) or AC (dark) stacked.*

In addition to their stacking orders, bilayer graphene and thicker areas differ in the morphology of the stacking domains (cf. Figure 4.1**d,e**), which indicates two distinct formation mechanisms. Most notably, bilayer domains are smaller, triangular and relatively regular. Similar morphologies have been observed in free-standing bilayer graphene, both etched from graphene-on-SiC [107] and transferred from copper [106, 121], where they were linked to strain between the layers introduced during sample growth or fabrication. While uniform strain causes a moiré reconstruction (Fig. 4.4**a**), it is often energetically favorable to form domains of commensurate, optimal Bernal stacking. In this case, all strain is concentrated into the domain walls, thus forming dislocation lines [106, 107], as sketched in Fig. 4.4**b**. Upon close examination of Fig. 4.1**b**, the network of these domain walls is visible as dark lines in our bright-field measurements. These lines correspond to the patterns observed by Speck et al. [103]. Such domain walls were predicted to host topological edge states [108, 109], which has also been experimentally confirmed recently [110, 120, 122].

The size of the triangular domains shrinks for increasing uniform strain, while anisotropic strain causes domains elongated perpendicular to the strain axis. The observed average domain diameter of ~100–200 nm coincides well with relaxation of the 0.2% lattice mismatch between buffer layer and first graphene layer [123]. We thus conclude that the tri-

angular domains in bilayer graphene result from strain thermally induced during growth and from the lattice mismatch with the SiC substrate and are intrinsic to the growth process. The presence of elongated triangular domains indicates non-uniform strain due to pinning to defects and substrate steps. (See Chapter 7 for a more extensive treatment of the relation between the domain sizes and the lattice strain).

The larger, irregularly shaped domains that dominate trilayer and four-layer areas (Figure 4.1**d,g**) can be explained by nucleation kinetics. To test this hypothesis, we study EG samples where the growth was stopped shortly after the nucleation of bilayer areas to prevent their coalescence. The resulting small bilayer islands on monolayer terraces are shown in bright-field and dark-field conditions in Figure 4.4**c** and **d**, respectively. We observe that bilayer areas with a diameter below ~300 nm form single domains of constant stacking order (either bright or dark in Fig. 4.4**d**) and that AB and AC stacked bilayer islands occur in roughly equal number. This indicates that new layers nucleate below existing ones in one of the two Bernal stacking orders randomly [95, 96, 113]. At the elevated growth temperature, domain walls in the existing layers can easily move to the edge of the new island where they annihilate. As islands of different stacking grow and coalesce, new domain walls are formed where they meet (cf. Fig. 4.2**a**). This opens the interesting possibility to engineer the dislocation network by patterning the SiC substrate before graphene growth.

Figure 4.5: *Strain-induced triangular domains are also visible in the trilayer. They are formed between the two bottom-most layers and are, hence, only visible at certain energies. At 33 eV ABA stacked areas appear dark (e.g. marked by a brown arrow) and ABC domains bright (e.g. pink arrow). This assignment can be made from the dark-field reflectivity spectra shown in Figure 4.2**d**. The same area as in Figure 4.1**d,g** is shown with areas of different layer number outlined in yellow. The same dark-field alignment as in Figure 4.1**d–f** is used here.*

33.0 eV

1 μm
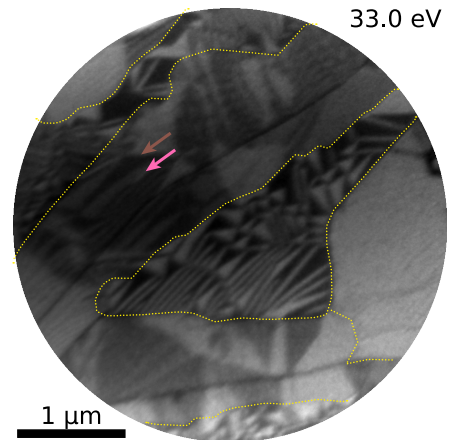
Notably, we observe strain-induced domains also in monolayer EG (Figure 4.4**d**) and between the bottom two layers in trilayer QFG (visible only for some energies, e.g. $E_0 =$ 33 eV in Figure 4.5). The prevalence of these triangular domains in all EG and QFG samples between the two bottommost layers demonstrates that stacking domains are a direct consequence of the epitaxial graphene growth and consequently are a general feature of this material system. The resulting domain wall network explains the linear magnetoresistance observed in bilayer QFG [8] and might be an important culprit for the generally low mobility in EG and QFG [44].

4.3.3 INFLUENCE ON HYDROGEN DE-INTERCALATION

The presence of these strain-induced domains in EG as well as QFG raises the question of their role during (hydrogen) intercalation. Since the high hydrogen pressures necessary for intercalation are not compatible with in situ imaging, we investigate the inverse process. Figure 4.6**a,** shows a time series of bright-field LEEM images of the area shown in Figure 4.1**b** recorded at ~1000 °C (cf. Supplementary Movie 3). At this temperature, hydrogen slowly leaves the SiC–graphene interface [44, 45] and n-layer QFG is transformed back to $n - 1$ layer (+ buffer layer) EG. The change in the reflectivity spectrum accompanied with this conversion (cf. Figure 4.3) yields strong contrast (e.g. dark in the bilayer in Figure 4.6**a**) and enables capture of the full deintercalation dynamics. Deintercalation starts at distinct point-like defect sites where hydrogen can escape and proceeds
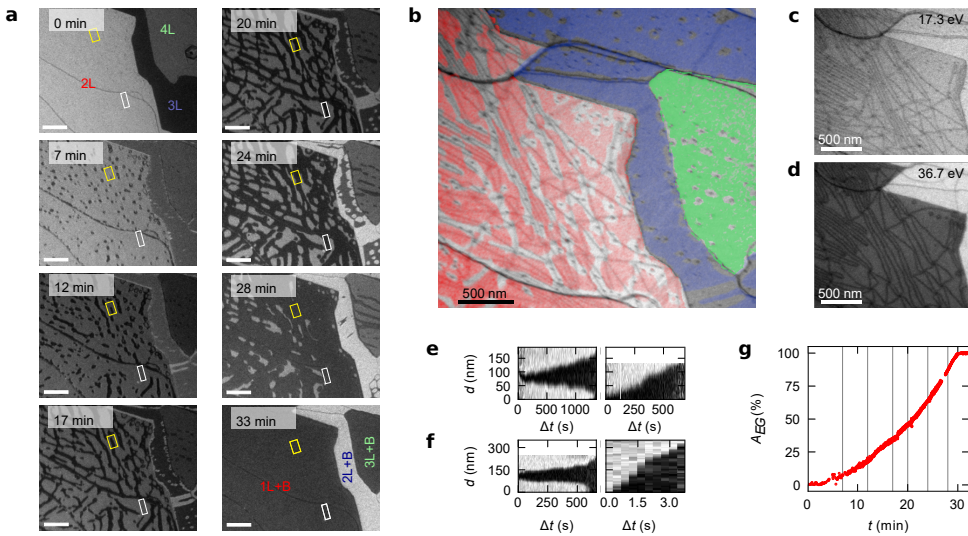

Figure 4.6: The hydrogen deintercalation dynamics is dominated by the graphene dislocation network. a, *Bright-field LEEM snapshots (E = 2.2 eV) of hydrogen deintercalation at ~1000 °C (the full time series is available as Supplementary Movie 3). Deintercalation starts in distinct points and deintercalated areas (dark in the bilayer region) grow in a strongly anisotropic fashion. Scale bars are 500 nm.* **b,** *Overlay of the deintercalation state at 15 min with a LEEM image showing the dislocation network (dark lines) beforehand. It reveals that deintercalation proceeds faster along dislocation lines. Areas shaded in color are still intercalated, while hydrogen is already removed in the uncolored areas.* **c, d,** *Bright-field images comparing the domain boundaries before and after deintercalation, respectively. While some dislocations move slightly, the overall features remain unchanged during the process.* **a** *to* **d** *show the same area as Fig. 4.1***b***.* **e,** *Slices along the time axis, perpendicular (left) and parallel (right) to the dislocation line marked yellow in* **a***, illustrate the velocity of the deintercalation front.* **f,** *Same for the dislocation marked white in* **a***. The movement of all deintercalation fronts is roughly linear in time and much faster parallel to dislocation lines than perpendicular.* **g,** *The fraction of deintercalated area A_{EG} extracted from the bilayer area in* **a** *grows non-linearly in time, indicating that the process is limited by the desorption of hydrogen at the boundary between intercalated and deintercalated areas.*

in a highly anisotropic fashion. An overlay of the half deintercalated state (15 min) with an image of the dislocations in the initial surface (Figure 4.6**b**) shows that deintercalation happens preferentially along dislocation lines. Although the dislocation lines are slightly mobile at higher temperatures (cf. Figure 4.6**c,d**) before and after deintercalation, respectively), their overall direction and density is preserved during the process. The local deintercalation dynamics reveal details of the underlying microscopic mechanism. Figure 4.6**e,f,** show that deintercalation fronts move roughly linearly in time both perpendicular and parallel to dislocation lines. The velocity of the deintercalation fronts however, is much larger parallel to dislocation lines (up to $v_\parallel = 95\,\mathrm{nm\,s^{-1}}$), than perpendicular to them ($v_\perp \approx 0.1\,\mathrm{nm\,s^{-1}}$). The linear movement rules out that deintercalation is limited by hydrogen diffusion, but indicates that hydrogen desorption at the deintercalation front is the limiting factor. The non-linear growth of the fraction of deintercalated area A_{EG} (Figure 4.6**g**) demonstrates that deintercalation is also not capped by the venting of hydrogen from the defects where deintercalation starts (7 min in Figure 4.6**a**). We conclude from these observations that the hydrogen desorption barrier is smaller within the domain walls than within the Bernal-stacked domains, possibly triggered by the higher lattice strain in the former. While $v_\perp$ is the same for all areas, $v_\parallel$ varies from $0.2\,\mathrm{nm\,s^{-1}}$ to $95\,\mathrm{nm\,s^{-1}}$ (marked yellow and white in Figure 4.6**a**, respectively), suggesting that the deintercalation process is strongly affected by the precise atomic details of the domain walls. These findings indicate that not only the deintercalation, but also the intercalation of hydrogen and other species, which all can not penetrate graphene, is dominated by the presence of stacking domains. Consequently, their manipulation, e.g. by patterning the substrate, will open a route towards improved intercalation and tailored QFG on the wafer-scale.

4.4 CONCLUSION

We conclude that graphene on SiC is a much richer material system than has been realized to this date. Specifically, we show that domains of AB and AC Bernal stacking orders are always present in this material, even for high quality argon-grown samples, and even though its layers appear perfectly crystalline to most methods. We deduce that these domains are formed between the two bottommost carbon layers (either graphene and buffer layer for EG or bilayer QFG) by strain relaxation. In addition, the nucleation of grains of different stacking order during growth causes larger domains in thicker layers. We show that dislocation lines between domains dominate hydrogen deintercalation dynamics, highlighting their importance for intercalation as well. By engineering these dislocation networks, we foresee wide implications for customized QFG for electronic applications. Moreover, the dislocation networks observed here could yield a wafer-scale platform for topological [108–110, 120, 122] and possibly strongly correlated electron phenomena [4, 111, 112] when tailored into periodic structures.

REFERENCES

4. Y. Cao, V. Fatemi, S. Fang, et al. Unconventional superconductivity in magic-angle graphene superlattices. *Nature* **556,** 43–50. doi:10.1038/nature26160 (2018).

6. J. Kautz, J. Jobst, C. Sorger, et al. Low-Energy Electron Potentiometry: Contactless Imaging of Charge Transport on the Nanoscale. *Scientific Reports* **5,** 13604. doi:10.1038/srep13604 (2015).

7. S.-H. Ji, J. B. Hannon, R. M. Tromp, et al. Atomic-scale transport in epitaxial graphene. *Nature Materials* **11,** 114–119. doi:10.1038/nmat3170 (2012).

8. F. Kisslinger, C. Ott, C. Heide, et al. Linear magnetoresistance in mosaic-like bilayer graphene. *Nature Physics* **11,** 650–653. doi:10.1038/nphys3368 (2015).

26. S. Schramm, J. Kautz, A. Berghaus, et al. Low-energy electron microscopy and spectroscopy with ESCHER: Status and prospects. *IBM Journal of Research and Development* **55,** 1–1. doi:10.1147/JRD.2011.2150691 (2011).

30. H. Hibino, H. Kageshima, F. Maeda, et al. Microscopic thickness determination of thin graphite films formed on SiC from quantized oscillation in reflectivity of low-energy electrons. *Physical Review B* **77,** 075413. doi:10.1103/PhysRevB.77.075413 (2008).

34. J. Jobst, A. J. H. van der Torren, E. E. Krasovskii, et al. Quantifying electronic band interactions in van der Waals materials using angle-resolved reflected-electron spectroscopy. *Nature Communications* **7,** 13621. doi:10.1038/ncomms13621 (2016).

37. T. A. de Jong, E. E. Krasovskii, C. Ott, et al. Intrinsic stacking domains in graphene on silicon carbide: A pathway for intercalation. *Physical Review Materials* **2,** 104005. doi:10.1103/PhysRevMaterials.2.104005 (2018).

38. J. Jobst, J. Kautz, D. Geelen, R. M. Tromp & S. J. van der Molen. Nanoscale measurements of unoccupied band dispersion in few-layer graphene. *Nature Communications* **6,** 8926. doi:10.1038/ncomms9926 (2015).

44. F. Speck, J. Jobst, F. Fromm, et al. The quasi-free-standing nature of graphene on H-saturated SiC(0001). *Applied Physics Letters* **99,** 122106. doi:10.1063/1.3643034 (2011).

45. C. Riedl, C. Coletti, T. Iwasaki, A. A. Zakharov & U. Starke. Quasi-Free-Standing Epitaxial Graphene on SiC Obtained by Hydrogen Intercalation. *Physical Review Letters* **103,** 246804. doi:10.1103/PhysRevLett.103.246804 (2009).

46. R. M. Feenstra, N. Srivastava, Q. Gao, et al. Low-energy electron reflectivity from graphene. *Physical Review B* **87,** 041406. doi:10.1103/PhysRevB.87.041406 (2013).

47. H. Hibino, S. Mizuno, H. Kageshima, M. Nagase & H. Yamaguchi. Stacking domains of epitaxial few-layer graphene on SiC(0001). *Physical Review B* **80,** 085406. doi:10.1103/PhysRevB.80.085406 (2009).

89. C. R. Eddy & D. K. Gaskill. Silicon Carbide as a Platform for Power Electronics. *Science* **324,** 1398–1400. doi:10.1126/science.1168704 (2009).

90. Y.-M. Lin, C. Dimitrakopoulos, K. A. Jenkins, et al. 100-GHz Transistors from Wafer-Scale Epitaxial Graphene. *Science* **327,** 662–662. doi:10.1126/science.1184289 (2010).

91. A. Tzalenchuk, S. Lara-Avila, A. Kalaboukhov, et al. Towards a quantum resistance standard based on epitaxial graphene. *Nature Nanotechnology* **5,** 186–189. doi:10.1038/nnano.2009.474 (2010).

92. S. Hertel, D. Waldmann, J. Jobst, et al. Tailoring the graphene/silicon carbide interface for monolithic wafer-scale electronics. *Nature Communications* **3,** 957. doi:10.1038/ncomms1955 (2012).

93. F. Bianco, D. Perenzoni, D. Convertino, et al. Terahertz detection by epitaxial-graphene field-effect-transistors on silicon carbide. *Applied Physics Letters* **107,** 131104. doi:10.1063/1.4932091 (2015).

94. C. Virojanadara, M. Syväjarvi, R. Yakimova, et al. Homogeneous large-area graphene layer growth on 6 H-SiC (0001). *Physical Review B* **78,** 245403. doi:10.1103/PhysRevB.78.245403 (2008).

95. K. V. Emtsev, A. Bostwick, K. Horn, et al. Towards wafer-size graphene layers by atmospheric pressure graphitization of silicon carbide. *Nature Materials* **8,** 203–207. doi:10.1038/nmat2382 (2009).

96. W. A. de Heer, C. Berger, M. Ruan, et al. Large area and structured epitaxial graphene produced by confinement controlled sublimation of silicon carbide. *Proceedings of the National Academy of Sciences* **108,** 16900–16905. doi:10.1073/pnas.1105113108 (2011).

97. Y.-M. Lin, A. Valdes-Garcia, S.-J. Han, et al. Wafer-Scale Graphene Integrated Circuit. *Science* **332,** 1294–1297. doi:10.1126/science.1204428 (2011).

98. K. V. Emtsev, A. A. Zakharov, C. Coletti, S. Forti & U. Starke. Ambipolar doping in quasifree epitaxial graphene on SiC(0001) controlled by Ge intercalation. *Physical Review B* **84,** 125423. doi:10.1103/PhysRevB.84.125423 (2011).

99. R. Nandkishore, L. S. Levitov & A. V. Chubukov. Chiral superconductivity from repulsive interactions in doped graphene. *Nature Physics* **8,** 158–163. doi:10.1038/nphys2208 (2012).

100. Y. Li, P. Tang, P. Chen, et al. Topological insulators in transition-metal intercalated graphene: The role of d electrons in significantly increasing the spin-orbit gap. *Physical Review B* **87,** 245127. doi:10.1103/PhysRevB.87.245127 (2013).

101. J. Baringhaus, A. Stöhr, S. Forti, U. Starke & C. Tegenkamp. Ballistic bipolar junctions in chemically gated graphene ribbons. *Scientific Reports* **5,** 9955. doi:10.1038/srep09955 (2015).

102. N. A. Anderson, M. Hupalo, D. Keavney, M. C. Tringides & D. Vaknin. Intercalated europium metal in epitaxial graphene on SiC. *Physical Review Materials* **1,** 054005. doi:10.1103/PhysRevMaterials.1.054005 (2017).

103. F. Speck, M. Ostler, S. Besendörfer, et al. Growth and Intercalation of Graphene on Silicon Carbide Studied by Low-Energy Electron Microscopy. *Annalen der Physik* **529,** 1700046. doi:10.1002/andp.201700046 (2017).

104. V. Berry. Impermeability of graphene and its applications. *Carbon* **62,** 1–10. doi:10.1016/j.carbon.2013.05.052 (2013).

105. S. Hu, M. Lozada-Hidalgo, F. C. Wang, et al. Proton transport through one-atom-thick crystals. *Nature* **516,** 227–230. doi:10.1038/nature14015 (2014).

106. J. S. Alden, A. W. Tsen, P. Y. Huang, et al. Strain solitons and topological defects in bilayer graphene. *Proceedings of the National Academy of Sciences* **110,** 11256–11260. doi:10.1073/pnas.1309394110 (2013).

107. B. Butz, C. Dolle, F. Niekiel, et al. Dislocations in bilayer graphene. *Nature* **505,** 533–537. doi:10.1038/nature12780 (2014).

108. I. Martin, Y. M. Blanter & A. F. Morpurgo. Topological Confinement in Bilayer Graphene. *Physical Review Letters* **100,** 036804. doi:10.1103/PhysRevLett.100.036804 (2008).

109. X. Li, F. Zhang, Q. Niu & A. H. MacDonald. Spontaneous layer-pseudospin domain walls in bilayer graphene. *Physical Review Letters* **113,** 116803. doi:10.1103/PhysRevLett.113.116803 (2014).

110. L. Ju, Z. Shi, N. Nair, et al. Topological valley transport at bilayer graphene domain walls. *Nature* **520,** 650–655. doi:10.1038/nature14364 (2015).

111. B. Hunt, J. D. Sanchez-Yamagishi, A. F. Young, et al. Massive Dirac Fermions and Hofstadter Butterfly in a van der Waals Heterostructure. *Science* **340,** 1427–1430. doi:10.1126/science.1237240 (2013).

112. Y. Cao, V. Fatemi, A. Demir, et al. Correlated insulator behaviour at half-filling in magic-angle graphene superlattices. *Nature* **556,** 80–84. doi:10.1038/nature26154 (2018).

113. S. Tanaka, K. Morita & H. Hibino. Anisotropic layer-by-layer growth of graphene on vicinal SiC(0001) surfaces. *Physical Review B* **81,** 041406. doi:10.1103/PhysRevB.81.041406 (2010).

114. R. M. Tromp & J. B. Hannon. Thermodynamics and Kinetics of Graphene Growth on SiC(0001). *Physical Review Letters* **102,** 106104. doi:10.1103/PhysRevLett.102.106104 (2009).

115. P. Lauffer, K. V. Emtsev, R. Graupner, et al. Atomic and electronic structure of few-layer graphene on SiC(0001) studied with scanning tunneling microscopy and spectroscopy. *Physical Review B* **77,** 155426. doi:10.1103/PhysRevB.77.155426 (2008).

116. E. E. Krasovskii, F. Starrost & W. Schattke. Augmented Fourier components method for constructing the crystal potential in self-consistent band-structure calculations. *Physical Review B* **59,** 10504–10511. doi:10.1103/PhysRevB.59.10504 (1999).

117. E. E. Krasovskii. Augmented-plane-wave approach to scattering of Bloch electrons by an interface. *Physical Review B* **70,** 245322. doi:10.1103/PhysRevB.70.245322 (2004).

118. V. U. Nazarov, E. E. Krasovskii & V. M. Silkin. Scattering resonances in two-dimensional crystals with application to graphene. *Phys. Rev. B* **87,** 041405. doi:10.1103/PhysRevB.87.041405 (4 2013).

119.   D. A. Siegel, S. Y. Zhou, F. El Gabaly, et al. Three-fold diffraction symmetry in epi-
       taxial graphene and the SiC substrate. *Physical Review B* **80,** 241407 (2009).

120.   H. Yoo, R. Engelke, S. Carr, et al. Atomic and electronic reconstruction at the van
       der Waals interface in twisted bilayer graphene. *Nature Materials* **18,** 448–453.
       doi:10.1038/s41563-019-0346-z (2019).

121.   L. Brown, R. Hovden, P. Huang, et al. Twinning and Twisting of Tri- and Bilayer
       Graphene. *Nano Letters* **12,** 1609–1615. doi:10.1021/nl204547v (2012).

122.   L.-J. Yin, H. Jiang, J.-B. Qiao & L. He. Direct imaging of topological edge states at a
       bilayer graphene domain wall. *Nature Communications* **7,** 11760. doi:10.1038/n
       comms11760 (2016).

123.   T. Schumann, M. Dubslaff, M. H. Oliveira, et al. Effect of buffer layer coupling on
       the lattice parameter of epitaxial graphene on SiC(0001). *Physical Review B* **90,**
       041403. doi:10.1103/PhysRevB.90.041403 (2014).